

Reversed flow at low frequencies in a microfabricated AC electrokinetic pump

Misha Marie Gregersen, Laurits Højgaard Olesen, Anders Brask, Mikkel Fougt Hansen, and Henrik Bruus

MIC – Department of Micro and Nanotechnology, Technical University of Denmark

DTU bldg. 345 east, DK-2800 Kongens Lyngby, Denmark

(Dated: 29 Marts 2007)

Microfluidic chips have been fabricated to study electrokinetic pumping generated by a low voltage AC signal applied to an asymmetric electrode array. A measurement procedure has been established and followed carefully resulting in a high degree of reproducibility of the measurements. Depending on the ionic concentration as well as the amplitude of the applied voltage, the observed direction of the DC flow component is either forward or reverse. The impedance spectrum has been thoroughly measured and analyzed in terms of an equivalent circuit diagram. Our observations agree qualitatively, but not quantitatively, with theoretical models published in the literature.

I. INTRODUCTION

The recent interest in AC electrokinetic micropumps was initiated by experimental observations by Green, Gonzales *et al.* of fluid motion induced by AC electroosmosis over pairs of microelectrodes [1, 2, 3] and by a theoretical prediction by Ajdari that the same mechanism would generate flow above an electrode array [4]. Brown *et al.* [5] demonstrated experimentally pumping of electrolyte with a low voltage, AC biased electrode array, and soon after the same effect was reported by a number of other groups observing flow velocities of the order of mm/s [6, 7, 8, 9, 10, 11, 12, 13]. Several theoretical models have been proposed parallel to the experimental observations [14, 15, 16]. However, so far not all aspects of the flow-generating mechanisms have been explained.

Studer *et al.* [10] made a thorough investigation of flow dependence on electrolyte concentration, driving voltage and frequency for a characteristic system. In this work a reversal of the pumping direction for frequencies above 10 kHz and rms voltages above 2 V was reported. For a travelling wave device Ramos *et al.* [12] observed reversal of the pumping direction at 1 kHz and voltages above 2 V. The reason for this reversal is not yet fully understood and the goal of this work is to contribute with further experimental observations of reversing flow for other parameters than those reported previously.

An integrated electrokinetic AC driven micropump has been fabricated and studied. The design follows Studer *et al.* [10], where an asymmetric array of electrodes covers the channel bottom in one section of a closed pumping loop. Pumping velocities are measured in another section of the channel without electrodes. In this way electrophoretic interaction between the beads used as flow markers and the electrodes is avoided. In contrast to the soft lithography utilized by Studer *et al.*, we use more well-defined MEMS fabrication techniques in Pyrex glass. This results in a very robust system, which exhibits stable properties and remains functional over time periods extending up to a year. Furthermore, we have a larger electrode coverage of the total channel length allowing for the detection of smaller pumping velocities. Our improved design has led to the observation of a new phe-

nomenon, namely the reversing of the flow at low voltages and low frequencies. The electrical properties of the fabricated microfluidic chip have been investigated to clarify whether these reflect the reversal of the flow direction. In accordance with the electrical measurements we propose and evaluate an equivalent circuit diagram. Supplementary details related to the present work can be found in Ref. [17].

II. EXPERIMENTAL

A. System design

The microchip was fabricated for studies of the basic electrokinetic properties of the system. Hence, a simple microfluidic circuit was designed to eliminate potential side-effects due to complex device issues. The chip consists of two 500 μm thick Pyrex glass wafers anodically bonded together. Metal electrodes are defined on the bottom wafer and channels are contained in the top wafer, as illustrated schematically in Fig. 1(a). This construction ensures an electrical insulated chip with fully transparent channels.

An electrode geometry akin to the one utilized by Brown *et al.* [5] and Studer *et al.* [10] was chosen. The translation period of the electrode array is 50 μm with electrode widths of $W_1 = 4.2 \mu\text{m}$ and $W_2 = 25.7 \mu\text{m}$, and corresponding electrode spacings of $G_1 = 4.5 \mu\text{m}$ and $G_2 = 15.6 \mu\text{m}$, see Fig. 1(d). Further theoretical investigations have shown that this geometry results in a nearly optimal flow velocity [16]. The total electrode array consists of eight sub-arrays each having their own connection to the shared contact pad, Fig. 1(b). This construction makes it possible to disconnect a malfunctioning sub-array. The entire electrode array has a width of 1.3 mm ensuring that the alignment of the electrodes and the 1.0 mm wide fluidic channels is not critical.

A narrow side channel, Fig. 1(b), allows beads to be introduced into the part of the channel without electrodes, where a number of ruler lines with a spacing of 200 μm enable flow measurements by particle tracing, Fig. 1(c).

An outer circuit of valves and tubes is utilized to con-

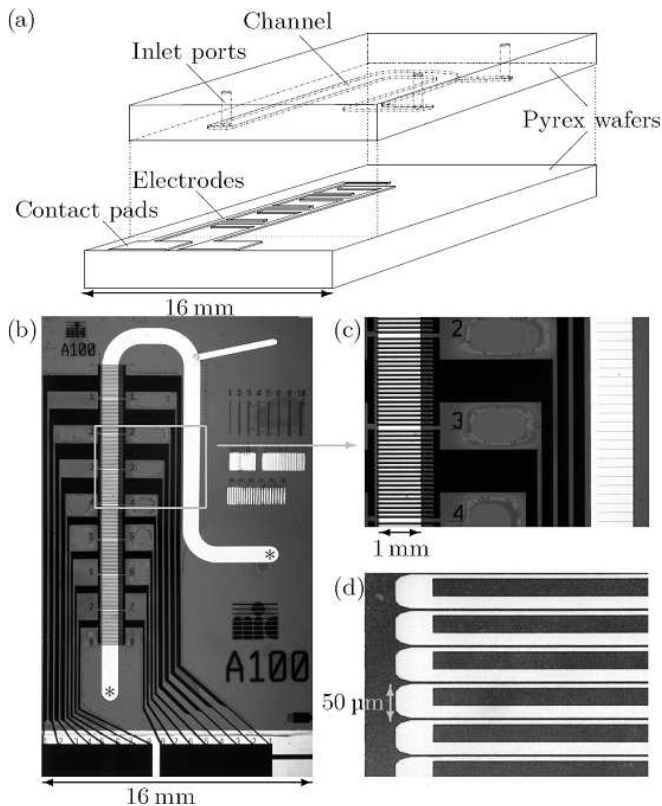


FIG. 1: (a) Sketch of the fabricated chip consisting of two Pyrex glass wafers bonded together. The channels are etched into the top wafer, which also contains the fluid access ports. Flow-generating electrodes are defined on the bottom wafer. (b) Micrograph of the full chip containing a channel (white) with flow-generating electrodes (black) and a narrow side channel for bead injection (upper right corner). During flow measurements the channel ends marked with an asterisk are connected by an outer tube. The electrode array is divided into eight sub arrays, each having its own connection to the electrical contact pad. (c) Magnification of the framed area in panel (b) showing the flow-generating electrodes to the left and the measurement channel with ruler lines to the right. (d) Close up of an electrode array section with electrode translation period of $50 \mu\text{m}$.

control and direct electrolytes and bead solutions through the channels. During flow-velocity measurements, the inlet to the narrow side channel is blocked and to eliminate hydrostatic pressure differences the two ends of the main channel are connected by an outer teflon tube with an inner diameter of 0.5 mm . The hydraulic resistance of this outer part of the pump loop is three orders of magnitude smaller than the on-chip channel resistance and is thus negligible.

The maximal velocity of the Poiseuille flow in the measurement channel section is denoted v_{pois} , and the average slip velocity generated above the electrodes by electroosmosis is denoted v_{slip} . To obtain a measurable v_{pois} at as low applied voltages as possible, the electrode coverage of the total channel length is made as large

Channel height	H	$33.6 \mu\text{m}$
Channel width	w	$967 \mu\text{m}$
Channel length	L_{tot}	40.8 mm
Channel length with electrodes	L_{el}	16.0 mm
Width of electrode array	w_{el}	$1300 \mu\text{m}$
Narrow electrode gap	G_1	$4.5 \mu\text{m}$
Wide electrode gap	G_2	$15.6 \mu\text{m}$
Narrow electrode width	W_1	$4.2 \mu\text{m}$
Wide electrode width	W_2	$25.7 \mu\text{m}$
Electrode thickness	h	$0.40 \mu\text{m}$
Electrode surface area ($[W_1 + 2h]w$)	A_1	$4.84 \times 10^{-9} \text{ m}^2$
Electrode surface area ($[W_2 + 2h]w$)	A_2	$25.63 \times 10^{-9} \text{ m}^2$
Number of electrode pairs	p	312
Electrode resistivity (Pt)	ρ	$10.6 \times 10^{-8} \Omega\text{m}$
Electrolyte conductivity (0.1 mM)	σ	1.43 mS/m
Electrolyte conductivity (1.0 mM)	σ	13.5 mS/m
Electrolyte permittivity	ϵ	$80 \epsilon_0$
Pyrex permittivity	ϵ_{p}	$4.6 \epsilon_0$

TABLE I: Dimensions and parameters of the fabricated microfluidic system.

as possible. In our system the total channel length is $L_{\text{tot}} = 40.8 \text{ mm}$ and the section containing electrodes is $L_{\text{el}} = 16.0 \text{ mm}$, which ensures a high Poiseuille flow velocity, $v_{\text{pois}} = (3/4)(L_{\text{el}}/L_{\text{tot}})v_{\text{slip}} = 0.29 v_{\text{slip}}$ [17].

The microfluidic chip has a size of approximately $16 \text{ mm} \times 28 \text{ mm}$ and is shown in Fig. 1, and the device parameters are listed in Table I.

B. Chip fabrication

The flow-generating electrodes of e-beam evaporated Ti(10 nm)/Pt(400 nm) were defined by lift-off in $1.5 \mu\text{m}$ thick photoresist AZ 5214-E (Hoechst) using a negative process. The Ti layer ensures good adhesion to the Pyrex substrate. Platinum is electrochemically stable and has a low resistivity, which makes it suitable for the application. By choosing an electrode thickness of $h = 400 \text{ nm}$, the metallic resistance between the contact pads and the channel electrolyte is at least one order of magnitude smaller than the resistance of the bulk electrolyte covering the electrode array.

In the top Pyrex wafer the channel of width $w = 967 \mu\text{m}$ and height $H = 33.6 \mu\text{m}$ was etched into the surface using a solution of 40% hydrofluoric acid. A 100 nm thick amorphous silicon layer was sputtered onto the wafer surface and used as etch mask in combination with a $2.2 \mu\text{m}$ thick photoresist layer. The channel pattern was defined by a photolithography process akin to the process used for electrode definition, and the wafer backside and edges were protected with a $70 \mu\text{m}$ thick etch resistant PVC foil. The silicon layer was then etched away in the channel pattern using a mixture of nitric acid and buffered hydrofluoric acid, $\text{HNO}_3:\text{BHF}:\text{H}_2\text{O} =$

20:1:20. The wafer was subsequently baked at 120°C to harden the photoresist prior to the HF etching of the channels. Since the glass etching is isotropic, the channel edges were left with a rounded shape. However, this has only a minor impact on the flow profile, given that the channel aspect ratio is $w/H \approx 30$. The finished wafer was first cleaned in acetone, which removes both the photoresist and the PVC foil, and then in a piranha solution.

After alignment of the channel and the electrode array, the two chip layers were anodically bonded together by heating the ensemble to 400°C and applying a voltage difference of 700 V across the two wafers for 10 min. During this bonding process, the previously deposited amorphous Si layer served as diffusion barrier against the sodium ions in the Pyrex glass. Finally, immersing the chip in DI-water holes were drilled for the in- and outlet ports using a cylindrical diamond drill with a diameter of 0.8 mm.

C. Measurement setup and procedures

Liquid injection and electrical contact to the microchip was established through a specially constructed PMMA chip holder, shown in Fig. 2. Teflon tubing was fitted into the holder in which drilled channels provided a connection to the on-chip channel inlets. The interface from the chip holder to the chip inlets was sealed by O-rings. Electrical contact was obtained with spring loaded contact pins fastened in the chip holder and pressed against the electrode pads. The inner wires of thin coax cables were soldered onto the pins and likewise fastened to the holder.

The pumping was induced by electrolytic solutions of KCl in concentrations ranging from $c = 0.1$ mM to 1.0 mM. The chip was prepared for an experiment by careful injection of this electrolyte into the channel and tubing system, after which the three valves to in- and outlets were closed. The electrical impedance spectrum of the microchip was measured before and after each series of flow measurements to verify that no electrode damaging had occurred during the experiments. If the

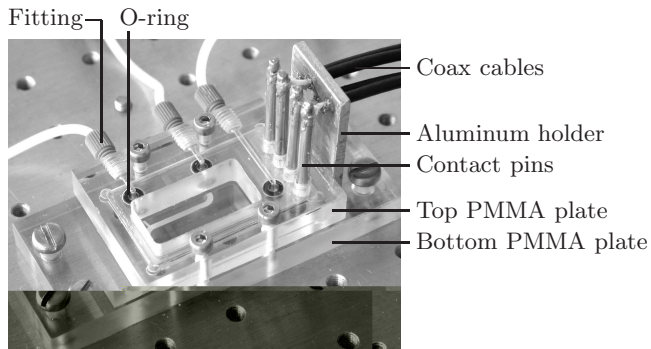


FIG. 2: Chip holder constructed to connect external tubing and electrical wiring with the microfluidic chip.

impedance spectrum had changed, the chip and the series of performed measurements were discarded. Velocity measurements were only carried out when the tracer beads were completely at rest before biasing the chip, and it was always verified that the beads stopped moving immediately after switching off the bias. The steady flow was measured for 10 s to 30 s. After a series of measurements was completed, the system was flushed thoroughly with milli-Q water. When stored in milli-Q water between experiments the chips remained functional for at least one year.

D. AC biasing and impedance measurements

Using an impedance analyzer (HP 4194 A), electrical impedance spectra of the microfluidic chip were obtained by four-point measurements, where each contact pad was probed with two contact pins. Data was acquired from 100 Hz to 15 MHz. To avoid electrode damaging by application of a too high voltage at low frequencies, all impedance spectra were measured at $V_{\text{rms}} = 10$ mV.

The internal sinusoidal output signal of a lock-in amplifier (Stanford Research SR830DSP) was used for AC biasing of the electrode array during flow-velocity measurements. The applied rms voltages were in the range from 0.5 V to 2 V and the frequencies between 0.5 kHz and 100 kHz. A current amplification was necessary to maintain the correct potential difference across the electrode array, since the overall chip resistance could be small (~ 0.1 k Ω to 1 k Ω) when frequencies in the given interval were applied. The current through the microfluidic chip was measured by feeding the output signal across a small series resistor back into the lock-in amplifier.

The lock-in amplifier was also used for measuring impedance spectra for frequencies below 100 Hz, which were beyond the span of the impedance analyzer.

E. Flow velocity measurements

After filling the channel with an electrolyte and actuating the electrodes, the flow measurements were performed by tracing beads suspended in the electrolyte.

Fluorescent beads (Molecular Probes, FluoSpheres F-8765) with a diameter of 1 μm were introduced into the measurement section of the channel and used as flow markers for the velocity determination. A stereo microscope was focused at the beads, and with an attached camera pictures were acquired with time intervals of $\Delta t = 0.125$ s to 1.00 s depending on the bead velocity. Subsequently, the velocity was determined by averaging over a distance of $\Delta x = 200$ μm , i.e., $v = \Delta x / \Delta t$. Only the fastest beads were used for flow detection, since these are assumed to be located in the vertical center of the channel. It should be noted that the use of fluorescent particles prevented an introduction of significant illumination heating of the sample.

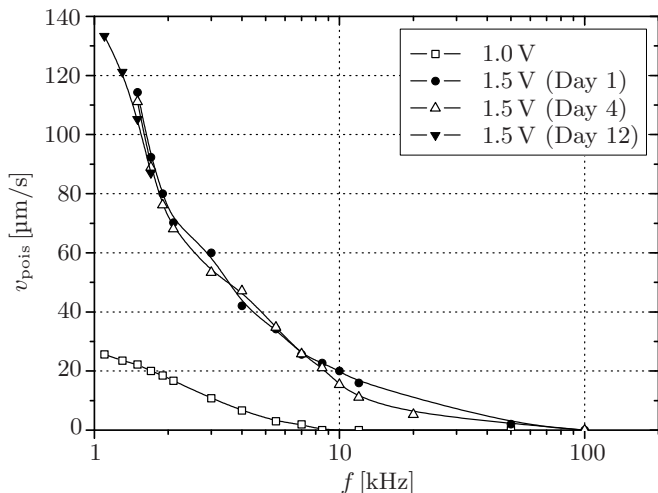


FIG. 3: Reproducible flow-velocities induced in a 0.1 mM KCl solution and observed at different days as a function of frequency at a fixed rms voltage of 1.5 V. A corresponding series was measured at $V_{\text{rms}} = 1.0$ V. Lines have been added to guide the eye.

The limited number of acquired pictures led to an uncertainty of 5% in the determination of flow velocities, which corresponds to the movement of the tracer beads within 0.5 to 1 frame. Additionally, there is a statistical uncertainty on the vertical particle position in the channel, which is estimated to introduce up to 10% error on the determined bead velocity. It is then assumed that the fastest beads are positioned within $H/3$ of the maximum of the Poiseuille flow profile.

III. RESULTS

In the parameter ranges corresponding to those published in the literature, our flow velocity measurements are in agreement with previously reported results. Using a $c = 0.1$ mM KCl solution and driving voltages of $V_{\text{rms}} = 1.0$ V to 1.5 V over a frequency range of $f = 1.1$ kHz to 100 kHz, we observed among other measurement series the pumping velocities shown in Fig. 3. The general tendencies were an increase of velocity towards lower frequencies and higher voltages, and absence of flow above $f \sim 100$ kHz. The measured velocities corresponded to slightly more than twice those measured by Studer *et al.* [10] due to our larger electrode coverage of the total channel. We observed damaging of the electrodes if more than 1 V was applied to the chip at a driving frequency below 1 kHz, for which reason there are no measurements at these frequencies. It is, however, plausible that the flow velocity for our chip peaked just below $f \sim 1$ kHz.

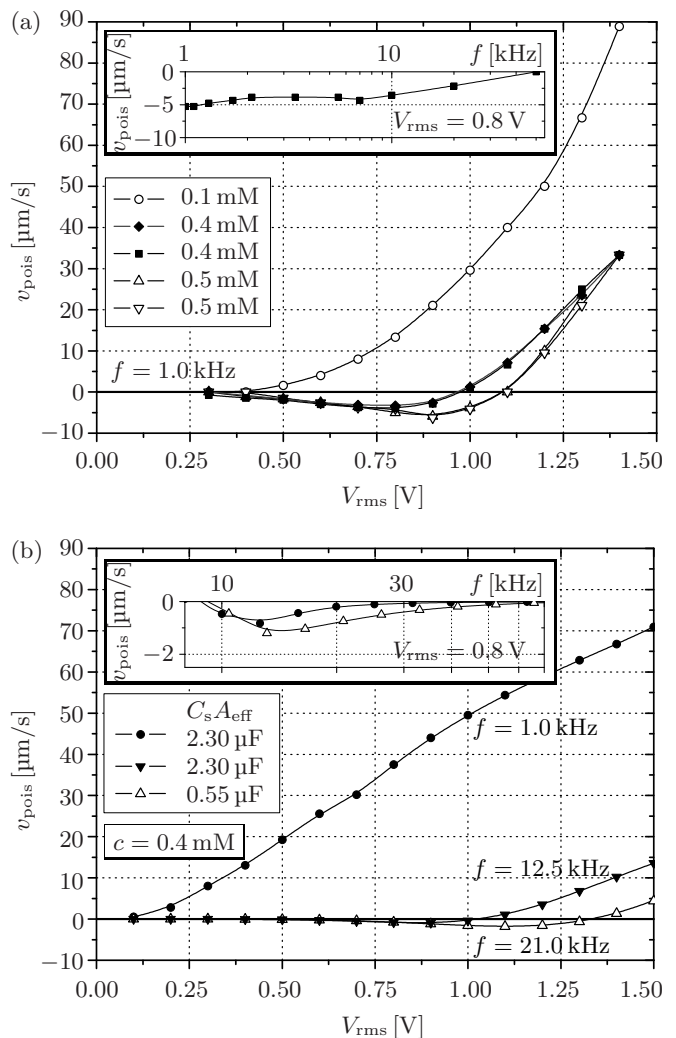


FIG. 4: (a) Reversed flow observed for repeated measurements of two concentrations of KCl at 1.0 kHz. The inset shows that for a 0.4 mM KCl solution at a fixed rms voltage of 0.8 V the flow direction remains negative, but slowly approaches zero for frequencies up to 50 kHz. (b) The theoretical model presented in Ref. [19] predicts the trends of the experimentally observed velocity curves. The depicted graphs are calculated for a $c = 0.4$ mM solution and parameters corresponding to the experiments (Table III) with $\zeta_{\text{eq}} = 160$ mV. Additional curves have been plotted for slightly different parameter values in order to obtain a closer resemblance to the experimental graphs, see Sec. IV.

A. Reproducibility of measurements

Our measured flow velocities were very reproducible due to the employed MEMS chip fabrication techniques and the careful measurement procedures described in Sec. II. This is illustrated in Fig. 3, which shows three velocity series recorded several days apart. The measurements were performed on the same chip and for the same parameter values. Between each series of measurements, the chip was dismantled and other experiments

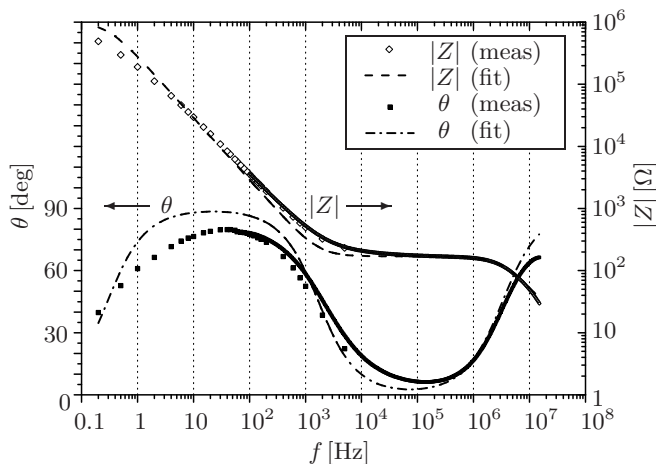


FIG. 5: Bode plot showing the measured amplitude $|Z|$ (right ordinate axis) and phase θ (left ordinate axis) of the impedance as a function of frequency over eight decades from 0.2 Hz to 15 MHz. The voltage was $V_{\text{rms}} = 10$ mV and the electrolyte concentration $c = 1.0$ mM KCl. The measurements are shown with symbols while the curves of the fitted equivalent diagram are represented by dashed lines. The measurement series obtained with the Impedance Analyzer consist of 400 very dense points while the series measured using the lock-in amplifier contains fewer points with a clear spacing.

performed. However, it should be noted that a very slow electrode degradation was observed when a dozen of measurement series were performed on the same chip over a couple of weeks.

B. Low frequency reversed flow

Devoting special attention to the low-frequency ($f < 20$ kHz), low-voltage regime ($V_{\text{rms}} < 2$ V), not studied in detail previously, we observed an unanticipated flow reversal for certain parameter combinations. Fig. 4(a) shows flow velocities measured for a frequency of 1.0 kHz as a function of applied voltage for various electrolyte concentrations. It is clearly seen that the velocity series of $c = 0.1$ mM exhibits the known exclusively forward and increasing pumping velocity as function of voltage, whereas for slightly increased electrolyte concentrations an unambiguous reversal of the flow direction is observed for rms voltages below approximately 1 V.

This reversed flow direction was observed for all frequencies in the investigated spectrum when the electrolyte concentration and the rms voltage were kept constant. This is shown in the inset of Fig. 4(a), where a velocity series was obtained over the frequency spectrum for an electrolyte concentration of 0.4 mM at a constant rms voltage of 0.8 V. It is noted that the velocity is nearly constant over the entire frequency range and tends to zero above $f \sim 20$ kHz.

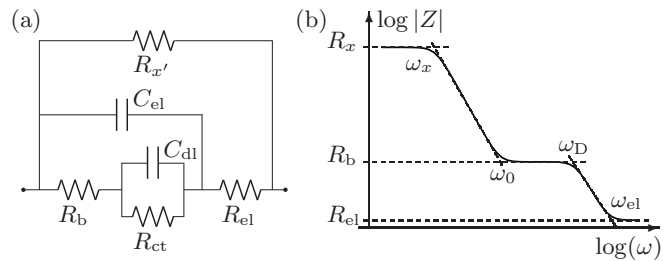


FIG. 6: (a) Equivalent circuit diagram. (b) Sketch of the impedance amplitude curve of the equivalent diagram. It consists of three plateaus, and four characteristic frequencies ω_x , ω_0 , ω_D and ω_{el} (see Table II) that characterize the shape and may be utilized to estimate the component values.

C. Electrical characterization

To investigate whether the flow reversal was connected to unusual properties of the electrical circuit, we carefully measured the impedance spectrum $Z(f)$ of the microfluidic system. Spectra were obtained for the chip containing KCl electrolytes with the different concentrations $c = 0.1$ mM, 0.4 mM and 1.0 mM.

Fig. 5 shows the Bode plots of the impedance spectrum obtained for $c = 1.0$ mM. For frequencies between $f \sim 1$ Hz and $f \sim 10^3$ Hz the curve shape of the impedance amplitude $|Z|$ is linear with slope -1 , after which a horizontal curve section follows, and finally the slope again becomes -1 for frequencies above $f \sim 10^6$ Hz. Correspondingly, the phase θ changes between 0° and 90° . From the decrease in phase towards low frequencies it is apparent that $|Z|$ must have another horizontal curve section below $f \sim 1$ Hz. When the curve is horizontal and the phase is 0° the system behaves resistively, while it is capacitively dominated when the phase is 90° and the curve has a slope of -1 .

Debye length	λ_D
Total electrode resistance	R_{el}
Total bulk electrolyte resistance	R_b
Total faradaic (charge transfer) resistance	R_{ct}
Internal resistance in lock-in amplifier	$R_{x'}$
Total measured resistance for $\omega \rightarrow 0$	R_x
Total electrode capacitance	C_{el}
Total double layer capacitance	C_{dl}
Debye layer capacitance	C_D
Surface capacitance	C_s
Debye frequency	ω_D
Inverse ohmic relaxation time	ω_0
Inverse faradaic charge transfer time (primarily)	ω_x
Characteristic frequency of electrode circuit	ω_{el}

TABLE II: List of the symbols used in the equivalent circuit model.

	R_b mod	R_b meas	R_{el} mod	R_{el} meas	R_{ct} meas	C_{dl} mod	C_{dl} meas	C_{el} mod	C_{el} meas	ω_D mod	ω_D meas	ω_0 mod	ω_0 meas
	[k Ω]	[k Ω]	[Ω]	[Ω]	[M Ω]	[μ F]	[μ F]	[nF]	[nF]	[M rad s $^{-1}$]		[k rad s $^{-1}$]	
0.1 mM (A)	2.0	1.0	7.6	5	1.0	0.50	0.50	0.28	0.30	2.0	3.3	1.0	2.0
1.0 mM (A)	0.21	0.17	7.6	6	1.0	0.56	0.55	0.28	0.29	19.1	20.6	8.5	10.7
0.1 mM (B)	2.0	1.4	7.6	6	–	0.50	0.51	0.28	0.29	2.0	3.0	1.0	1.4
0.4 mM (B)	0.52	0.41	7.6	7	–	0.54	0.53	0.28	0.28	7.7	9.3	3.6	4.6
1.0 mM (B)	0.21	0.17	7.6	8	–	0.56	0.55	0.28	0.26	19.1	22.6	8.5	10.5

TABLE III: Comparison of measured (meas) and modeled (mod) values of the components in the equivalent diagram, Fig. 6. The measured values are given by curve fits of Bode plots, Fig. 5, obtained on two similar chips labeled A and B, respectively. The modeled values are estimated on basis of Table I and a particular choice of the parameters ζ_{eq} and C_s . This choice is not unique since different combinations can lead to the same value of C_{dl} .

D. Equivalent circuit

In electrochemistry the standard way of analyzing such impedance measurements is in terms of an equivalent circuit diagram [20]. The choice of diagram is not unambiguous [3]. We have chosen the diagram shown in Fig. 6(a) with the component labeling listed in Table II.

Charge transport through the bulk electrolyte is represented by an ohmic resistance R_b , accumulation of charge in the double layer at the electrodes by a capacitance C_{dl} , and faradaic current injection from electrochemical reactions at the electrodes by another resistance, the charge-transfer resistance R_{ct} [16, 20]. Moreover, we include the ohmic resistance of the metal electrodes R_{el} , the mutual capacitance between the narrow and wide electrodes C_{el} , and a shunt resistance $R_{x'} = 10$ M Ω to represent the internal resistance of the lock-in amplifier.

Finally, in electrochemical experiments at low frequency, the electrical current is often limited by diffusive transport of the reactants in the faradaic electrode reaction to and from the electrodes. This can be modeled by adding a frequency dependent Warburg impedance in series with the charge transfer resistance [20]. However, because the separation between the electrodes is so small and the charge transfer resistance is so large, we are unable to distinguish the Warburg impedance in the impedance measurements and leave it out of the equivalent diagram.

By fitting the circuit model to the impedance measurements we extract the component values listed in Table III. On the chip labeled B we were unable to measure the charge transfer resistance due to a minor error on the chip introduced during the bonding process. Fig. 6(b) illustrates the relation between component values and the impedance amplitude curve through four characteristic angular frequencies $\omega = 2\pi f$. The inverse frequency $\omega_x^{-1} = R_x C_{dl}$ primarily expresses the characteristic time for the faradaic charge transfer into the Debye layer. The characteristic time for charging the Debye layer through the electrolyte is given by $\omega_0^{-1} = R_b C_{dl}$. The Debye frequency is $\omega_D = 1/(R_b C_{el})$, and finally $\omega_{el} = 1/(R_{el} C_{el})$ simply states the characteristic frequency for the on-chip

electrode circuit in the absence of electrolyte. It is noted that the total DC-limit resistance R_x corresponds to the parallel coupling between $R_{x'}$ and R_{ct} .

IV. DISCUSSION

In the following we investigate to which extent the general theory of induced-charge (AC) electroosmosis can explain our observations and experimental data. We first use the equivalent circuit component values extracted from the impedance measurements to estimate some important electrokinetic parameters based on the Gouy–Chapman–Stern model [20], namely, the Stern layer capacitance C_s , the intrinsic zeta potential ζ_{eq} on the electrodes and the charge transfer resistance R_{ct} . Then we use this as input to the weakly nonlinear electrohydrodynamic model presented in Ref. [19], which is an extension of the model in Ref. [16]. We compare theoretical values with experimental observations, and discuss the experimentally observed trends of the flow velocities.

A. Impedance analysis

The impedance measurements are performed at a low voltage of $V_{rms} = 10$ mV so it might be expected that Debye–Hückel linear theory applies ($V \lesssim 25$ mV). However, since we only measure the potential difference between the electrodes and we do not know the potential of the bulk electrolyte, we cannot say much about the exact potential drop across the double layer. Many electrode-electrolyte systems possess an intrinsic zeta potential at equilibrium ζ_{eq} of up to a few hundred mV. Indeed, the measured C_{dl} is roughly 10 times larger than predicted by Debye–Hückel theory, which indicates that the intrinsic zeta potential is at least ± 125 mV.

According to Gouy–Chapman–Stern theory the C_{dl} can be expressed as a series coupling of the compact Stern layer capacitance C_s and the differential Debye-layer ca-

capacitance C_D ,

$$\frac{A_{\text{eff}}}{C_{\text{dl}}} = \frac{1}{C_s} + \frac{1}{C_D}, \quad (1)$$

where the two double-layer capacitances of an electrode pair are coupled in series through the electrolyte, and since the p electrode pairs are coupled in parallel, the effective area of the total double layer is $A_{\text{eff}} = p A_1 A_2 / (A_1 + A_2)$. A_1 and A_2 are the total surface areas exposed to the electrolyte of a narrow and wide electrode, respectively. For simplicity C_s is often assumed constant and independent of potential and concentration, while C_D is given by the Gouy–Chapman theory as

$$C_D = \frac{\epsilon}{\lambda_D} \cosh\left(\frac{\zeta_{\text{eq}} z e}{2k_B T}\right). \quad (2)$$

Unfortunately, it is not possible to estimate the exact values of both C_s and ζ_{eq} from a measurement of C_{dl} , because a range of parameters lead to the same C_{dl} . We can, nevertheless, state lower limits as $C_s \geq 0.39 \text{ F/m}^2$ and $|\zeta_{\text{eq}}| \geq 175 \text{ mV}$ for $c = 0.1 \text{ mM}$ or $C_s \geq 0.43 \text{ F/m}^2$ and $|\zeta_{\text{eq}}| \geq 125 \text{ mV}$ at $c = 1.0 \text{ mM}$.

For the model values in Table III we used Eq. (1) with $C_s = 1.8 \text{ F/m}^2$ and $\zeta_{\text{eq}} = 190 \text{ mV}$, 160 mV and 140 mV at 0.1 mM , 0.4 mM and 1.0 mM KCl, respectively, in accordance with the trend often observed that ζ_{eq} decreases with increasing concentration, [21]. The bulk electrolyte resistance can be expressed as

$$R_b = \frac{0.85}{\sigma w p}, \quad (3)$$

where σ is the conductivity, w is the width of the electrodes and p is the number of electrode pairs, see Table I, and 0.85 is a numerical factor computed for our particular electrode layout using the finite-element based program COMSOL MULTIPHYSICS. Similarly, the mutual capacitance between the electrodes can be calculated as

$$C_{\text{el}} = \frac{p}{0.85} [\epsilon w + \epsilon_p (2w_{\text{el}} - w)], \quad (4)$$

and the resistance R_{el} of the electrodes leading from the contact pads to the array is simply estimated from the resistivity of platinum and the electrode geometry.

At frequencies above 100 kHz the impedance is dominated by R_b , C_{el} and R_{el} , and the Bode plot closely resembles a circuit with ideal components, see Fig. 5. Around 1 kHz we observe some frequency dispersion which could be due to the change in electric field line pattern around the inverse RC-time $\omega_0 = 1/(R_b C_{\text{dl}})$ [19]. Finally, below 1 kHz where the impedance is dominated by C_{dl} , the phase never reaches 90° indicating that the double layer capacitance does not behave as an ideal capacitor but more like a constant phase element (CPE). This behavior is well known experimentally, but not fully understood theoretically [22].

B. Flow

The forward flow velocities measured at $c = 0.1 \text{ mM}$ as a function of frequency, Fig. 3, qualitatively exhibit the trends predicted by standard theory, namely, the pumping increases with voltage and falls off at high frequency [4, 14].

More specifically, the theory predicts that the pumping velocity should peak at a frequency around the inverse RC-time ω_0 , corresponding to $f \approx 0.3 \text{ kHz}$, and decay as the inverse of the frequency for our applied driving voltages, see Fig. 11 in Ref. [16]. Furthermore, the velocity is predicted to grow like the square of the driving voltage at low voltages, changing to $V \log V$ at large voltages [16, 19].

Experimentally, the velocity is indeed proportional to ω^{-1} and the peak is not observed within the range 1.1 kHz to 100 kHz, but it is likely to be just below 1 kHz. However, the increase in velocity between 1.0 V and 1.5 V displayed in Fig. 3 is much faster than V^2 . That is also the result in Fig. 4(a) for $c = 0.1 \text{ mM}$ where no flow is observed below $V_{\text{rms}} = 0.5 \text{ V}$, while above that voltage the velocity increases rapidly. For $c = 0.4 \text{ mM}$ and $c = 0.5 \text{ mM}$ the velocity even becomes negative at voltages $V_{\text{rms}} \leq 1 \text{ V}$. This cannot be explained by the standard theory and is also rather different from the reverse flow that has been observed by other groups at larger voltages $V_{\text{rms}} > 2 \text{ V}$ and at frequencies above the inverse RC-time [10, 12, 13].

The velocity shown in the inset of Fig. 4(a) is remarkable because it is almost constant between 1 kHz and 10 kHz. This is unlike the usual behavior for AC electroosmosis that always peaks around the inverse RC-time, because it depends on partial screening at the electrodes to simultaneously get charge and tangential field in the Debye layer. At lower frequency the screening is almost complete so there is no electric field in the electrolyte to drive the electroosmotic fluid motion, while at higher frequency the screening is negligible so there is no charge in the Debye layer and again no electroosmosis.

One possible explanation for the almost constant velocity as a function of frequency could be that the amount of charge in the Debye layer is controlled by a faradaic electrode reaction rather than by the ohmic current running through the bulk electrolyte. Our impedance measurement clearly shows that the electrode reaction is negligible at $f = 1 \text{ kHz}$ and $V_{\text{rms}} = 10 \text{ mV}$ bias, but since the reaction rate grows exponentially with voltage in an Arrhenius type dependence, it may still play a role at $V_{\text{rms}} = 0.8 \text{ V}$. However, previous theoretical investigations have shown that faradaic electrode reactions do not lead to reversal of the AC electroosmotic flow or pumping direction [16].

Due to the strong nonlinearity of the electrode reaction and the asymmetry of the electrode array, there may also be a DC faradaic current running although we drive the system with a harmonic AC voltage. In the presence of an intrinsic zeta potential ζ_{eq} on the electrodes and/or

the glass substrate this would give rise to an ordinary DC electroosmotic flow. This process does not necessarily generate bubbles because the net reaction products from one electrode can diffuse rapidly across the narrow electrode gap to the opposite electrode and be consumed by the reverse reaction.

To investigate to which extent this proposition applies, we used the weakly nonlinear theoretical model presented in [19]. The model extends the standard model for AC electroosmosis by using the Gouy–Chapman–Stern model to describe the double layer, and Butler–Volmer reaction kinetics to model a generic faradaic electrode reaction [20]. The concentration of the oxidized and reduced species in the diffusion layer near the electrodes is modeled by a generalization of the Warburg impedance, while the bulk concentration is assumed uniform, see Ref. [19] for details.

The model parameters are chosen in accordance with the result of the impedance analysis, i.e., $C_s = 1.8 \text{ F/m}^2$, $R_{ct} = 1 \text{ M}\Omega$, $\zeta_{eq} = 160 \text{ mV}$, as discussed in Sec. IV A. Further we assume an intrinsic zeta potential of $\zeta_{eq} = -100 \text{ mV}$ on the borosilicate glass walls [21], and choose (arbitrarily) an equilibrium bulk concentration of 0.02 mM for both the oxidized and the reduced species in the electrode reaction, which is much less than the KCl electrolyte concentration of $c = 0.4 \text{ mM}$.

The result of the model calculation is shown in Fig. 4(b). At 1 kHz the fluid motion is dominated by AC electroosmosis which is solely in the forward direction. However, at 12.5 kHz the AC electroosmosis is much weaker and the model predicts a (small) reverse flow due to the DC electroosmosis for $V_{rms} < 1 \text{ V}$.

Fig. 4(b) shows that the frequency interval with reverse flow is only from 30 kHz down to 10 kHz , while the measured velocities remain negative down to at least 1 kHz . The figure also shows results obtained with a lower Stern layer capacitance $C_s = 0.43 \text{ F/m}^2$ in the model, which turns out to enhance the reverse flow.

In both cases, the reverse flow predicted by the theoretical model is weaker than that observed experimentally and does not show the almost constant reverse flow profile below 10 kHz . Moreover, the model is unable to account for the strong concentration dependence displayed in Fig. 4(a).

According to Ref. [18], steric effects give rise to a significantly lowered Debye layer capacitance and a potentially stronger concentration dependence when ζ exceeds $10 k_B T/e \sim 250 \text{ mV}$, which roughly corresponds to a driving voltage of $V_{rms} \sim 0.5 \text{ V}$. Thus, by disregarding these effects we overestimate the double layer capacitance slightly in the calculations of the theoretical flow velocity for $V_{rms} = 0.8 \text{ V}$. This seems to fit with the observed tendencies, where theoretical velocity curves calculated on the basis of a lowered C_{dl} better resemble the measured curves.

Finally, it should be noted that several electrode reactions are possible for the present system. As an example we mention $2\text{H}_2\text{O}_{(l)} + \text{O}_{2(aq)} + 4e^- \rightleftharpoons 4\text{OH}^-_{(aq)}$. This reaction is limited by the amount of oxygen present in the solution, which in our experiment is not controlled. If this reaction were dominating the faradaic charge transfer, the value of R_{ct} could change from one measurement series to another.

V. CONCLUSION

We have produced an integrated AC electrokinetic micropump using MEMS fabrication techniques. The resulting systems are very robust and may preserve their functionality over years. Due to careful measurement procedures it has been possible over weeks to reproduce flow velocities within the inherent uncertainties of the velocity determination.

An hitherto unobserved reversal of the pumping direction has been measured in a regime, where the applied voltage is low ($V_{rms} < 1.5 \text{ V}$) and the frequency is low ($f < 20 \text{ kHz}$) compared to earlier investigated parameter ranges. This reversal depends on the exact electrolytic concentration and the applied voltage. The measured velocities are of the order $-5 \text{ }\mu\text{m/s}$ to $-10 \text{ }\mu\text{m/s}$. Previously reported studies of flow measured at the same parameter combinations show zero velocity in this regime [10]. The reason why we are able to detect the flow reversal is probably our design with a large electrode coverage of the channel leading to a relative high ratio $v_{pois}/v_{slip} = 0.29$.

Finally, we have performed an impedance characterization of the pumping devices over eight frequency decades. By fitting Bode plots of the data, the measured impedance spectra compared favorably with our model using reasonable parameter values.

The trends of our flow velocity measurements are accounted for by a previously published theoretical model, but the quantitative agreement is lacking. Most important, the predicted velocities do not depend on electrolyte concentration, yet the concentration seems to be one of the causes of our measured flow reversal, Fig. 4(a). This shows that there is a need for further theoretical work on the electro-hydrodynamics of these systems and in particular on the effects of electrolyte concentration variation.

Acknowledgments

We would like to thank Torben Jacobsen, Department of Chemistry (DTU), for enlightening discussions about electrokinetics and the interpretation of impedance measurements on electrokinetic systems.

-
- [1] N. G. Green, A. Ramos, A. Gonzalez, H. Morgan and A. Castellanos, *Phys. Rev. E* **61**(4), 4011 (2000).
- [2] A. Gonzalez, A. Ramos, N. G. Green, A. Castellanos and H. Morgan, *Phys. Rev. E* **61**(4), 4019 (2000).
- [3] N. G. Green, A. Ramos, A. Gonzalez, H. Morgan and A. Castellanos, *Phys. Rev. E* **66**, 026305 (2002).
- [4] A. Ajdari, *Phys. Rev. E* **61**, R45 (2000).
- [5] A. B. D. Brown, C. G. Smith and A. R. Rennie, *Phys. Rev. E* **63**, 016305 (2000).
- [6] V. Studer, A. Pépin, Y. Chen and A. Ajdari, *Microelectron. Eng.* **61-62**, 915 (2002).
- [7] M. Mpholo, C. G. Smith and A. B. D. Brown, *Sens. Actuators B* **92**, 262 (2003).
- [8] D. Lastochkin, R. Zhou, P. Whang, Y. Ben and H.-C. Chang, *J. Appl. Phys.* **96**, 1730 (2004).
- [9] S. Debesset, C. J. Hayden, C. Dalton, J. C. T. Eijkel and A. Manz, *Lab Chip* **4**, 396 (2004).
- [10] V. Studer, A. Pépin, Y. Chen and A. Ajdari, *The Analyst* **129**, 944 (2004).
- [11] B. P. Cahill, L. J. Heyderman, J. Gobrecht and A. Stemmer, *Phys. Rev. E* **70**, 036305 (2004).
- [12] A. Ramos, H. Morgan, N. G. Green, A. Gonzalez and A. Castellanos, *J. Appl. Phys.* **97**, 084906 (2005).
- [13] P. García-Sánchez, A. Ramos, N. G. Green and H. Morgan, *IEEE Trans. Dielect. El. In.* **13**, 670 (2006).
- [14] A. Ramos, A. Gonzalez, A. Castellanos, N. G. Green and H. Morgan, *Phys. Rev. E* **67**, 056302 (2003).
- [15] N. A. Mortensen, L. H. Olesen, L. Belmon and H. Bruus, *Phys. Rev. E* **71**, 056306 (2005).
- [16] L. H. Olesen, H. Bruus and A. Ajdari, *Phys. Rev. E* **73**, 056313 (2006).
- [17] M. M. Gregersen, *AC Asymmetric Electrode Micropumps*, MSc Thesis, MIC - Dept. of Micro and Nanotechnology, DTU (2005), www.mic.dtu.dk/mifts
- [18] M. S. Kilic, M. Z. Bazant and A. Ajdari, *Phys. Rev. E* **75**, 021502 (2007) and *Phys. Rev. E* **75**, 021503 (2007).
- [19] L. H. Olesen, *AC Electrokinetic micropumps*, PhD Thesis, MIC - Dept. of Micro and Nanotechnology, DTU (2006), www.mic.dtu.dk/mifts
- [20] A. J. Bard and L. R. Faulkner, *Electrochemical Methods*, 2. ed. (Wiley, 2001).
- [21] B. J. Kirby and E. F. Hasselbrink, *Electrophoresis* **25**, 187 (2004).
- [22] Z. Kerner and T. Pajkossy, *Electrochim. Acta* **46**, 207 (2000).